



Simulating planetary wave propagation to the upper atmosphere during stratospheric warming events at different mountain wave scenarios

Nikolai M. Gavrilov^{a,*}, Andrey V. Koval^a, Alexander I. Pogoreltsev^b, Elena N. Savenkova^a

^a Atmospheric Physics Department, Saint-Petersburg State University, Saint-Petersburg 198504, Russia

^b Meteorological Forecast Department, Russian State Hydrometeorological University, Saint-Petersburg 192007, Russia

Received 26 December 2016; received in revised form 11 July 2017; accepted 17 August 2017

Available online 30 August 2017

Abstract

Parameterization schemes of atmospheric normal modes (NMs) and orographic gravity waves (OGWs) have been implemented into the mechanistic Middle and Upper Atmosphere Model (MUAM) simulating atmospheric general circulation. Based on the 12-members ensemble of runs with the MUAM, a composite of the stratospheric warming (SW) has been constructed using the UK Met Office data as the lower boundary conditions. The simulation results show that OGW amplitudes increase at altitudes above 30 km in the Northern Hemisphere after the SW event. At altitudes of about 50 km, OGWs have largest amplitudes over North American and European mountain systems before and during the composite SW, and over Himalayas after the SW. Simulations demonstrate substantial (up to 50–70%) variations of amplitudes of stationary planetary waves (PWs) during and after the SW in the mesosphere-lower thermosphere of the Northern Hemisphere. Westward travelling NMs have amplitude maxima not only in the Northern, but also in the Southern Hemisphere, where these modes have waveguides in the middle and upper atmosphere. Simulated variations of PW and NM amplitudes correspond to changes in the mean zonal wind, EP-fluxes and wave refractive index at different phases of the composite SW events. Inclusion of the parameterization of OGW effects leads to decreases in amplitudes (up to 15%) of almost all SPWs before and after the SW event and their increase (up to 40–60%) after the SW in the stratosphere and mesosphere at middle and high northern latitudes. It is suggested that observed changes in NM amplitudes in the Southern Hemisphere during SW could be caused by divergence of increased southward EP-flux. This EP-flux increases due to OGW drag before SW and extends into the Southern Hemisphere.

© 2017 COSPAR. Published by Elsevier Ltd. All rights reserved.

Keywords: Circulation modeling; Middle and upper atmosphere; Planetary waves; Orographic gravity waves; Parameterization; Sudden stratospheric warming

1. Introduction

Transport of momentum and energy by internal waves is vital for the coupling dynamical processes in the lower (troposphere), middle (stratosphere-mesosphere) and upper (thermosphere) atmosphere (Andrews et al., 1987; Buhler, 2009; Pancheva et al., 2009). It is known that numerical

models of the thermal regime and general circulation of the middle atmosphere involve heating rates and drag of the mean flow created by decaying internal waves (Holton, 1975; McLandress et al., 2012). An important source of atmospheric waves is the relief of the Earth (Gossard and Hooke, 1975). Forcing of orographic gravity waves (OGWs) by atmospheric flows over mountains and the wave transfer of momentum and energy into the middle and upper atmosphere can substantially influence the general circulation, planetary waves (PWs) there, and can

* Corresponding author.

E-mail address: n.gavrilov@spbu.ru (N.M. Gavrilov).

provide dynamical coupling of different atmospheric layers. Numerical simulations of gravity wave (GW) impacts on the general circulation, tide amplitudes and their seasonal variations were performed, for instance, by [McLandress \(2002\)](#), [Gavrilov et al. \(2005\)](#), [Ortland and Alexander \(2006\)](#), [Watanabe and Miyahara \(2009\)](#), etc. Irregularities of gravity wave excitation and conditions of their propagation to the middle and upper atmosphere can create different PW modes (e.g., [Holton, 1984](#); [Mayr et al., 2011](#); [Hoffmann et al., 2012](#)).

Several studies were recently devoted to the peculiarities of interactions between planetary and internal gravity waves in the atmosphere (e.g., [McLandress and McFarlane, 1993](#); [Cohen et al., 2013, 2014](#); [Sigmond and Shepherd, 2014](#)). [Miyahara et al. \(1986\)](#) showed that PWs can influence GW propagation and GW drag may suppress stationary PWs in the winter mesosphere. [Yiğit and Medvedev \(2015\)](#) stressed that atmospheric waves generated by meteorological processes have a broad range of temporal and spatial scales, and may propagate to the middle and upper atmosphere. They showed that studies of SSWs and variability of the upper atmosphere could give information about dynamical coupling of the lower and upper atmosphere induced by the waves. Interactions PW with GWs in the middle and upper atmosphere were observed with different ground-based and satellite methods (e.g. [Ramesh et al., 2013](#); [Vincent, 2015](#)).

Simplified schemes exist for parameterizing dynamical and thermal OGW impacts (e.g., [Kim and Arakawa, 1995](#); [Lott and Miller, 1997](#); [Scinocca and McFarlane, 2000](#); [Vosper and Brown, 2007](#); [Cathy et al., 2008](#); [Geller et al., 2011](#)). Recently [Gavrilov et al. \(2013a\)](#) implemented a parameterization of dynamical and thermal effects of stationary OGWs into the mechanistic Middle and Upper Atmospheric Model (MUAM) simulating general circulation at altitudes from the troposphere up to the thermosphere. OGWs are supposed to affect the general atmospheric circulation in the middle and upper atmosphere. Additionally, [Gavrilov et al. \(2013b\)](#) simulated changes in the atmospheric PW amplitudes caused by OGWs. It was shown that taking account of OGW dynamical and thermal effects leads to changes (up to 50%) in amplitudes of stationary and westward propagating PWs.

Sudden stratospheric warming (SSW) event is one of the most remarkable processes of dynamical coupling between the troposphere and the middle atmosphere. These events involve rapid and strong temperature rises (up to 30–40 K) at altitudes about 30 km at high latitudes with related decreases, or even reversals, of climatological eastward mean zonal wind associated with polar night jets in the winter stratosphere (e.g., [McInturff, 1978](#); [McIntyre, 1982](#)). Breaking planetary waves that propagate upwards from the troposphere can contribute to the SSW development (e.g., [Quiroz, 1975](#); [Labitzke, 1977](#); [Schoeberl, 1978](#); [Nath et al., 2016](#)). The SSW events can substantially affect the dynamics and energetics of the upper atmosphere ([Siskind et al., 2010](#); [Kurihara et al., 2010](#); [Fuller-Rowell](#)

[et al., 2010](#); [Funke et al., 2010](#); [Liu et al., 2011](#); [Yuan et al., 2012](#)), i.e. they can influence the space weather.

There are some curious and remarkable results of analysis of SSW distinctive features obtained in recent years (e.g., [Labitzke et al., 2005](#); [Labitzke and Kunze, 2009](#); [Kuttippurath and Nikulin, 2012](#)). Despite the permanently increasing interest in the study of SSWs and their manifestation in the upper atmosphere and ionosphere, numerous questions still exist concerning the mechanisms of the SSW influencing wave propagation to the upper atmosphere.

Many observations of PWs and their changes during SSWs were made in the mesosphere and lower thermosphere (MLT) regions. These events were observed using ground-based radar (e.g., [Stray et al., 2015](#)) and optical (e.g., [Takahashi et al., 2006](#); [Reisin et al., 2014](#)) methods, as well as by satellite (e.g., [Pancheva et al., 2009](#)) data. PWs and their relations to SSWs were observed in different places and longitudes in the MLT ([Bittner et al., 2000](#); [Espy et al., 1997](#); [French and Burns, 2004](#); [Murphy et al., 2007](#); [Buriti et al., 2005](#); [López-González et al., 2009](#)). General variability caused by PWs ([Reisin et al., 2014](#)) and characteristics of different spectral components ([Takahashi et al., 2006](#); [Scheer et al., 1994](#); [Pancheva et al., 2008, 2009](#)) were studied. There are evidences for changes in the dynamical and wave processes in the mesosphere and thermosphere at not only high northern latitudes, but at middle and low latitudes also, and even in the Southern Hemisphere ([Goncharenko et al., 2012](#); [Sassi et al., 2013](#); [Fagundes et al., 2015](#); [Limpasuvan et al., 2016](#)).

In the present study, numerical simulations of PW propagation from the troposphere to the upper atmosphere at different latitudes during the composite stratospheric warming event have been performed. The parameterization of atmospheric normal modes (NMs) has been used in the MUAM with January–February climatological conditions and amplitudes of stationary PW modes and westward travelling NMs have been analyzed for time intervals before, during and after the composite stratospheric warming. Numerical experiments have been conducted including and excluding the parameterization scheme of OGW dynamical and thermal effects in the numerical model. Special interest is devoted to peculiarities of different PW and NM mode propagation to the upper atmosphere from below, their role in dynamical coupling of different atmospheric layers, their possible propagation across the equator and their influence on the mesosphere and lower thermosphere of both hemispheres during stratospheric warmings.

2. General circulation model and OGW parameterization

The idiom “sudden stratospheric warming” is usually associated with sharp temperature increases at the 10 hPa pressure level (e.g., [Butler et al., 2015](#)). In this study, using MUAM simulations we determined and investigated a number of similar phenomena at different altitudes between

30 and 60 km. To differentiate these phenomena from traditionally considered SSWs, we call them hereafter as “stratospheric warmings” (SWs).

To study planetary wave characteristics and OGW influence in the upper atmosphere during composite SW events, we performed numerical simulation of the general circulation with the MUAM described by Pogoreltsev (2007) and Pogoreltsev et al. (2007). The model is a modification of the COMMA general circulation model of Cologne University in Germany (Ebel et al., 1995). The MUAM solves the standard set of primitive equations in spherical coordinates. Calculations cover altitudes from the ground up to about 135 km. The regular horizontal grid spacing in the model is 5.6° along longitude and 5° in latitude. The vertical grid is equidistantly spaced in the log-pressure coordinate $z = H^* \ln(p_0/p)$, where p_0 is the surface pressure and $H = 7$ km is the average density scale height. This grid approximately corresponds to the geopotential height. In the present simulations, we used the MUAM version with 48 vertical levels (separated by 2.8 km), the integration time step was set to 450 s. The model involves three-dimensional ozone distribution in the middle atmosphere, which involves longitudinal inhomogeneities (Suvorova and Pogoreltsev, 2011).

In the lower atmosphere, the MUAM was initialized by geopotential height and temperature fields from the UK Met Office stratospheric assimilation data (Swinbank and O’Neill, 1994). As far as quasi-biennial oscillations (QBOs) in the equatorial stratosphere can influence atmospheric dynamics at middle and high latitudes, in this study we used averaged for January–February fields for all years with easterly QBO phases during years 1992–2011 taking into account the list of “easterly” and “westerly” years obtained by Inoue et al. (2011). These years are the same as were used in the previous publications (Gavrilov et al., 2013b, 2015) for better comparisons. The MUAM model can reproduce stationary planetary waves (SPWs) and propagating NMs (Pogoreltsev et al., 2014, 2015). At the lower boundary, SPW amplitudes are estimated from geopotential heights in the lower atmosphere obtained from the UK Met Office meteorological data mentioned above.

To parameterize NM sources in the MUAM, we added terms to the heat balance equation, which include sets of time-dependent sinusoidal components with zonal wavenumbers $m = 1$ and $m = 2$ and periods corresponding to simulated NMs. Latitude structures of these components are specified with respective Hough functions, using the method by Swarztrauber and Kasahara (1985). NM periods correspond to the resonant periods of atmospheric response to the wave forcing at low altitudes, which were determined with a linear planetary wave model by Pogoreltsev (1999). In the present study we consider the westward travelling NMs (1, 1), (1, 2), (2, 1) and (2, 2) in the classification by Longuet-Higgins (1968). They have the resonant periods of 4, 5, 7 and 10 days, respectively. We specified the same amplitudes of heating rates

$2 \cdot 10^{-5}$ K/s in forcing thermal sources for all NMs mentioned above. These sources provide amplitudes of simulated NM comparable with the observed ones in the stratosphere (Pogoreltsev et al., 2009).

The numerical modeling starts from an initial windless state having a UK Met Office temperature distribution for January–February and performs several stages of adjustment. During the first 30 model days, geopotential heights at the lower boundary are constant and OGW parameterization is not included. After day 31, we specified the observed variations of geopotential. In the course of the first 120–140 days, the MUAM uses only the daily averaged heating rates. The test runs (Pogoreltsev, 2007) showed that the described procedure allows the model to reach steady-state regime at the end of this time interval. Then daily variations of heating and an additional prognostic equation for the geopotential at the lower boundary are included. This prognostic equation needs to satisfy the lower boundary condition for the waves generated by internal sources. Starting from 330th model day, seasonal changes in solar heating are triggered and the next 60 days are considered as characteristic for January–February.

The SW development depends on the phases of stratospheric vacillations of wind and PW characteristics (e.g., Holton and Mass, 1976). In the MUAM, the vacillation phase depends on the time interval between the simulation start and the moment of triggering daily variations of solar heating during the described above adjustment process. In the present study, 12-member ensemble of the MUAM simulations were generated with triggering the diurnal variability of solar heating and prognostic equation for geopotential height at the lower boundary (Pogoreltsev et al., 2007, 2009) at different model days between 120 and 140. The NM parameterization is triggering at the same moments, which makes difference in NM phases for different MUAM runs.

Horizontal jet streams overflowing mountains produce disturbances of atmospheric parameters. In many cases, they may be qualified as internal OGWs (e.g. Gossard and Hooke, 1975). Propagation of these OGWs in the atmosphere leads to energy exchange between waves and the mean flow. Their dissipation plays an important role in the heating of the middle atmosphere. A parameterization of dynamical and thermal effects of stationary OGWs having zero ground-based observed frequency was developed by Gavrilov and Koval (2013). To calculate vertical profiles of the total vertical wave energy flux and associated accelerations of horizontal winds by stationary OGWs, the wave polarization relations were used. Correct implementation of these relations requires accounting for the atmosphere rotation. Analytical relations between the rate of wave energy dissipation and wave acceleration for nonzero vertical gradients of the mean wind were applied to describe the energy balance of the considered dynamical processes (see Gavrilov and Koval, 2013).

The parameterization of mesoscale topography uses the concept of “subgrid orography” (Scinocca and McFarlane,

2000). It involves the height variations of the Earth surface with much smaller horizontal scales than the horizontal grid spacing of the used numerical model. At the lower boundary, using the analysis of forces acting on the atmospheric flow moving over the effective elliptical mountain (Phillips, 1984), we determine OGW amplitude and effective horizontal wave number, which are used for computing the vertical profiles of wave acceleration and heat fluxes (Gavrilov and Koval, 2013).

Numerical experiments were performed for pairs of the MUAM runs with and without inclusion of the OGW parameterization. Spatial distributions of the zonal wind variations caused by PWs were simulated for 11-day time intervals before, during, and after the composite SW event. We analyzed SPW modes with zonal wave numbers $m = 1-4$ and westward propagating NMs having $m = 1$ and $m = 2$ with periods 5, 10 and 4, 7 days, respectively, and their changes due to OGW generation and propagation.

As discussed by Shaw and Shepherd (2007), improper gravity wave parameterization can produce non-conservation of angular momentum near the upper boundaries of general circulation models and spurious downward influences. Considered in the present study OGWs practi-

cally disappear below 90 km, while the MUAM has upper boundary at much higher altitudes about 135 km. Therefore, almost all effects of stationary OGWs occur within MUAM height domain and cannot produce artificial non-conservations of angular momentum.

3. Results of simulations

Simulations with the MUAM show existence of minor and/or major SW events at altitudes 20–60 km at high northern latitudes in all model runs for described above averaged climatological characteristics. To obtain average characteristics a set of 12 pairs of the MUAM runs having SWs with different phases of stratospheric vacillations and NM phases (see Section 2) were performed. To find dates of major and minor SWs we generally used the definitions by Charlton and Polvani (2007), however the zonal wind decreases and reversals were tested not only at the pressure level of 10 hPa, but at higher altitudes up to 60 km in each run (see an example in Fig. 1 and description in the next paragraph). Then we chose three 11-day intervals (referred as “before”, “during” and “after”) for each SW date and get respective SPW and NM amplitudes, EP-fluxes and

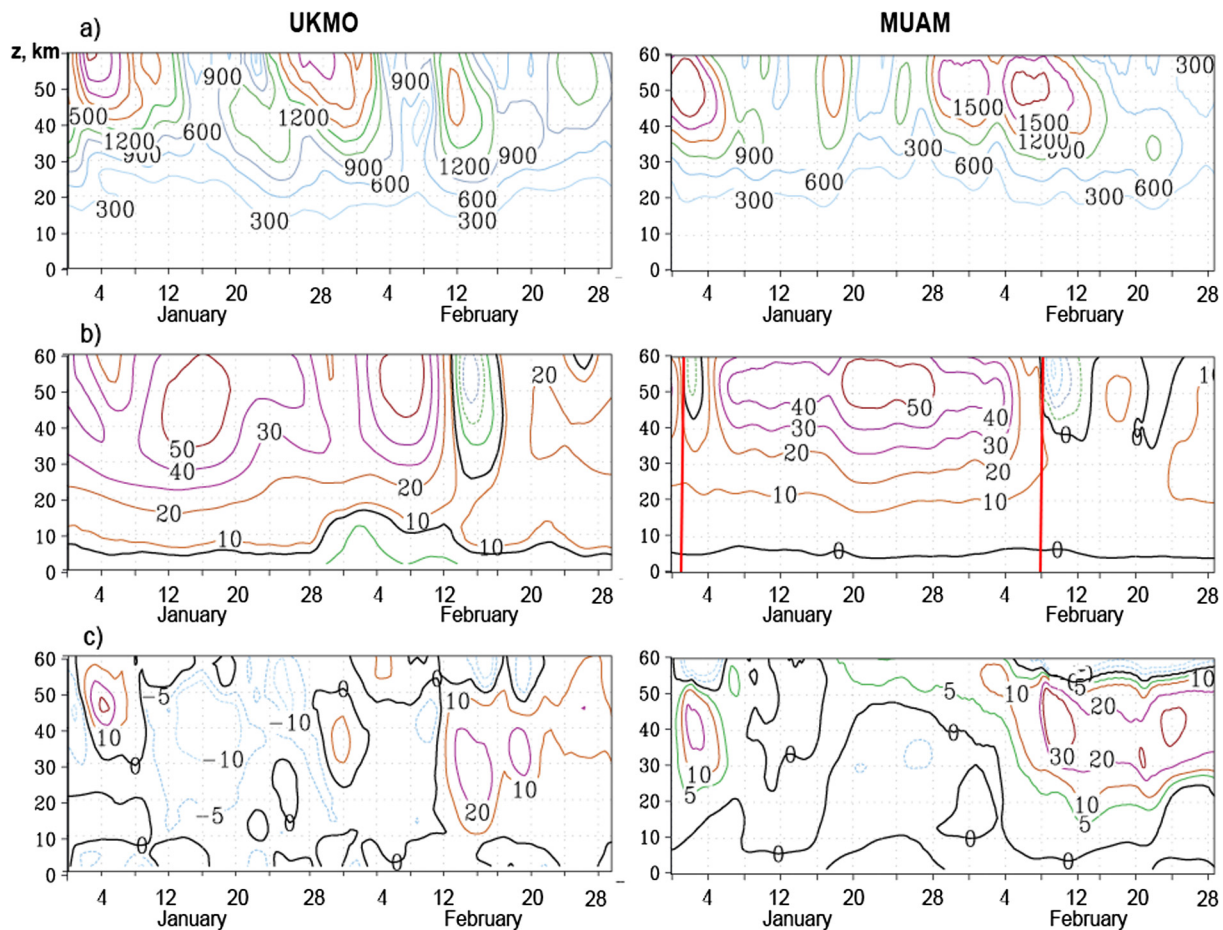


Fig. 1. Examples of obtained from the UK Met Office meteorological database for the year 2007 (left panels) and simulated with the MUAM including OGW parameterization (right panels) the geopotential height amplitude of SPW1 with zonal number $m = 1$ in gpm at latitude 62°N (a), zonal mean zonal wind in m/s at 62°N (b) and deviations of the zonal mean temperature from the two-month average in K at 87.5°N (c). Vertical lines mark the dates of simulated SW events.

refractive indices for each run separately. After that, we obtained characteristics averaged over ten MUAM runs for respective time intervals. All figures below are plotted for entire height range of the MUAM. However, one should keep in mind a possible influence of the upper boundary conditions at altitudes above 100 km.

3.1. Changes of the zonal mean characteristics

Fig. 1 shows an example of observed and simulated changes in the amplitude of geopotential height produced by PW with zonal wavenumber $m = 1$ and zonal mean zonal wind at latitude 62°N , also deviation of the zonal mean temperature from its two-month average at 87.5°N for the model time range January - February. Events similar to the right panels of Fig. 1 could be observed in the stratosphere. The left panels of Fig. 1 show an example obtained from the UK Met Office database of assimilation of stratospheric meteorological data for January–February 2007.

The right panels of Fig. 1b and c reveal two sharp increases in simulated high latitude temperature (up to 15–30 K) with simultaneous decreases in zonal velocity at altitudes above 30 km in early January and in the first half of February. One can also see respective zonal velocity reversals at altitudes above 40–45 km on January 1 and February 8 (marked with vertical lines in the right panel of Fig. 1b). These dates are considered as starting SW dates and 11-day intervals January 1–10 and February 8–18 are referred as “during SW” below. Other 11-day intervals referred as “before SW” and “after SW” are chosen with 5-day gaps before and after the mentioned above intervals, respectively. From plots similar to the right panels of Fig. 1 for 11 of 12 pairs of MUAM runs (with and without OGW parameterization), we choose 11-day intervals, which we refer as “before”, “during” and “after” the simulated SW events, respectively. Using the described method we determined 12 SW events (6 with OGW and 6 without OGW) having the zonal wind reversals. The other 12 SWs have significant temperature increases (at least 15 K) with no zonal wind reversals, which can be classified as minor SWs.

Both experimental and simulated results of Fig. 1a show increases in PW1 amplitudes in the upper stratosphere just before and during SW events and the amplitude decreases after them. In the right panel of Fig. 1b, one can observe significant weakening of zonal wind and its reversal in the stratosphere during SW event at latitude 62°N . The right panel of Fig. 1c shows that the increase in the simulated mean temperature during the composite SW can reach 20–30 K in the polar stratosphere.

Fig. 2 shows zonal wind, deviation of temperature from its two-month mean and OGW amplitude averaged for 11-day intervals before, during and after the composite SW, which are simulated with the MUAM including the OGW parameterization and averaged over longitude and 12 simulated SW events. The structure of zonal circulation simulated with the MUAM and presented in Fig. 2a gener-

ally corresponds to the existing empirical wind models (e.g., Jacobi et al., 2009; Pogoreltsev et al., 2009). The MUAM gives small westward zonal winds at altitudes 80–100 km at high northern latitudes, while empirical models give small eastward winds there (e.g. Hedin et al., 1996). The difference may be caused by excessive PW drag due to overestimating westward travelling NMs at the lower boundary in the MUAM.

When comparing the left, middle and right panels of Fig. 2, one can use statistical procedure of pairing samples comparing (e.g. Rice, 2006, chapter 11.3). From 12 SW events at each altitude and latitude for every pair of 11-day intervals, we have $12 \times 66 \times 64 = 50,688$ pairs of individual zonal wind and temperature values in 66 time (4-h outputs) and 64 longitude grid nodes. Estimations of standard deviations of differences between these pairs and application of paired Student t -test (e.g. Rice, 2006, chapter 11.3.1) gives 95% statistical reliability of the differences between the mean values showed in Fig. 2, if the differences exceed 1 m/s and 0.2 K for the zonal mean zonal wind (Fig. 2a) and the mean temperature deviations (Fig. 2b), respectively.

During SWs, in the middle panel of Fig. 2a, the maximum of the mean zonal wind at altitudes 50–70 km at the middle and high latitudes of the Northern Hemisphere becomes smaller and shifts to lower latitudes than those before SW in the left panel of Fig. 2a. After the composite SW, the northern strato-mesospheric jet speeds up again in the right panel of Fig. 2a. This corresponds to usually observed decreases and reversals of the mean eastward circulation in the high-latitude northern strato-mesosphere during SWs (see examples in Fig. 1). This behavior of the mean zonal wind is consistent with changes in the temperature meridional gradients, which influence the wind velocity in accordance with the thermal wind equation. Warmer polar stratosphere during the SW events corresponds to smaller temperature gradients directed to the equator, which decrease the velocity of the eastward atmospheric circulation. Cooling the polar stratosphere after the SW leads to increasing the equatorward temperature gradient and to the recovery of the mean eastward velocity in the polar stratosphere seen in Fig. 2a. Another reason may be displacement of Polar Vortex off the pole during SW (e.g., Palmeiro et al., 2015). The right plot of Fig. 2a shows smaller maximum velocities of the westward circulation in the southern strato-mesosphere after SW. As far as many of intervals after SW are near the end of February, these differences may be connected with seasonal changes in the circulations of the middle atmosphere.

Before the composite SW, in the left panel of Fig. 2b one can see a small maximum of temperature deviations near the North Pole at altitudes 60–70 km and a temperature minimum at altitudes 70–100 km. The maximum can reflect the middle atmosphere heating by northward heat fluxes produced by PWs near their amplitude maximum and discussed below. During SW, the middle panel of Fig. 2b shows warming near the North Pole with the average

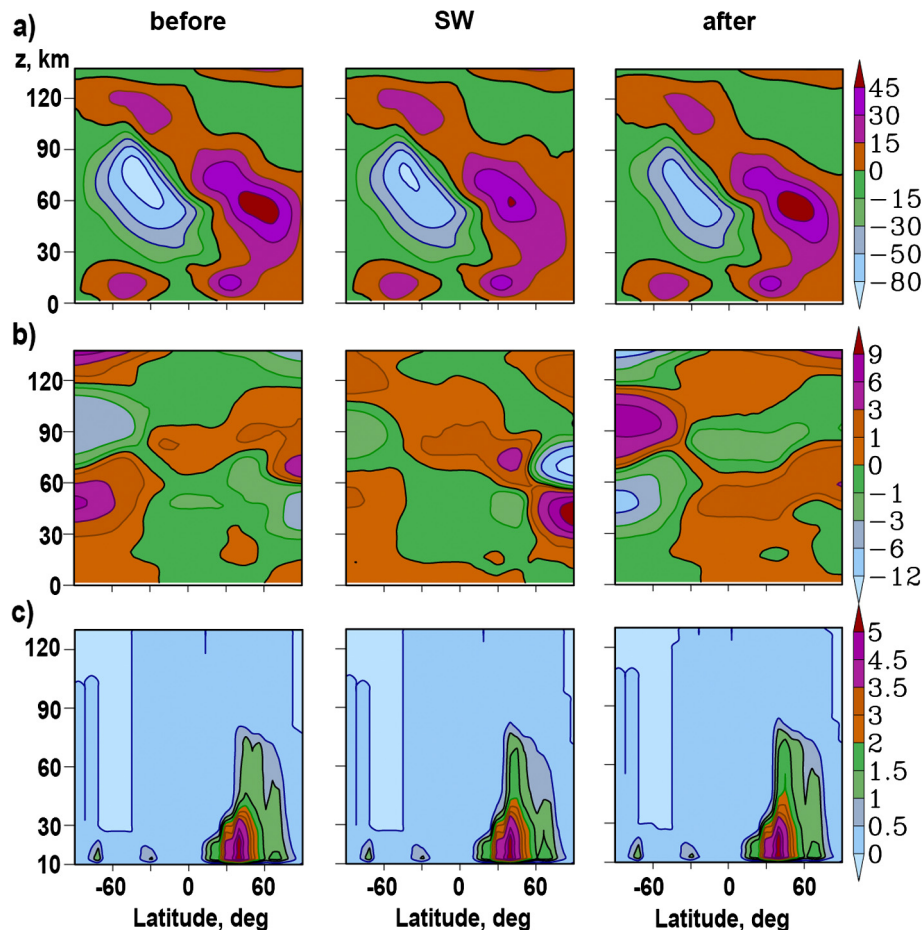


Fig. 2. Latitude-altitude distributions of the zonal mean zonal wind in m/s (a), deviation of the zonal mean temperature from the two-month average in K (b) and OGW velocity amplitudes in m/s (c) simulated with the MUAM and averaged over four 11-day time intervals before (left), during (middle) and after (right) the composite SW event. Thick contours show zero values.

temperature deviation reaching 13 K at altitudes 30–60 km, and cooling at altitudes 60–90 km with negative temperature deviation up to -13 K. After the composite SW, the right panel of Fig. 2b reveals weaker temperature deviation near the North Pole, but the polar stratosphere is still warmer and mesosphere is cooler than those before the composite SW. In the high-latitude Southern Hemisphere, Fig. 2b shows gradual increase in temperature at altitudes 70–110 km and temperature decrease at 30–70 km. A reason for these gradual temperature changes could be seasonal temperature changes leading to mentioned above transformations of the circulation in the Southern Hemisphere in the right panel of Fig. 2a. In the Northern Hemisphere, gradual seasonal temperature changes can superimpose the SW perturbations leading to differences between the left and right panels of Fig. 2b.

Fig. 2c reveals weakening of OGW amplitudes at altitudes above 40 km during SW and somewhat larger OGW amplitudes after SW. This can be caused by changes in OGW sources and conditions of their propagation in different SW stages.

Fig. 3 reveals Northern Hemisphere distributions of the same simulated characteristics as are shown in Fig. 2 at

fixed altitudes 30 and 50 km. For comparisons of pairs of 11-day intervals, one have at each latitude and longitude $12 \times 66 = 792$ pairs of individual values at 66 time instances for 12 simulated SW events. Estimations of standard deviations of differences between these pairs and application of paired Student t -test shows 95% statistical reliability of the differences between the mean values showed in Fig. 3, if the differences exceed 4 m/s and 0.5 K for the zonal mean zonal wind (Fig. 3a) and the mean temperature deviations (Fig. 3b), respectively.

Analysis of Fig. 3a shows two maxima of the eastward mean wind at altitude 50 km over North America and Siberia before SW. During SW, the wind becomes smaller over Eastern Europe and Western Siberia and the Siberian maximum shifts to the east closer to the North Pole. After the composite SW, eastward wind decreases, its maxima shifts towards Eurasia. Respective changes occur in the winds at lower altitudes, which could alter conditions of OGW generation and propagation over different mountain systems. Therefore, at altitude 50 km in Fig. 3c, OGWs generated by the North American and European mountain systems have largest amplitudes before SW, while OGWs over Himalayas become strongest after the SW event.

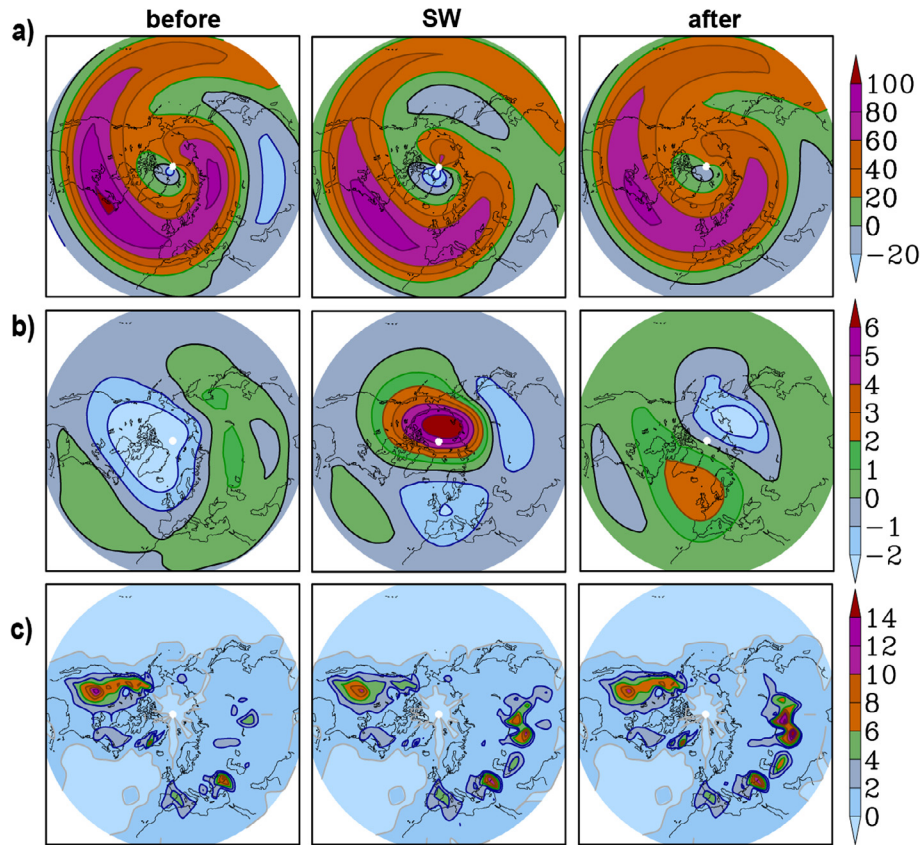


Fig. 3. Latitude-longitude distributions of zonal wind velocity at altitude 50 km in m/s (a), temperature at altitude 30 km in K (b) and OGW velocity amplitude at altitude 50 km in m/s (c) simulated with the MUAM and averaged over four 11-day time intervals before (left), during (middle) and after (right) the composite SW event. Thick contours show zero values.

The middle panel of Fig. 3b reveals significant temperature maximum at altitude 30 km near the North Pole during the composite SW, which corresponds to the respective panel of Fig. 2b. Similar distribution can be observed in the UKMO assimilation data during SW for year 2007.

3.2. Planetary wave amplitudes

To analyze possible relations between SW events and PWs, we made the least squares fitting longitude and time Fourier transform of meteorological fields simulated with the MUAM including OGW parameterization. We estimated amplitudes of stationary PWs with zonal numbers $m = 1-4$ (which we denote as SPW1–SPW4) and westward propagating NMs (see Section 2) as it was suggested by Fedulina et al. (2004) for each of 12 model runs and averaged these amplitudes over this ensemble.

Fig. 4 represents average geopotential height amplitudes of SPW1–SPW4 having zonal wave numbers $m = 1-4$ for time intervals before, during and after composite SW event. For comparisons, each pair of 11-day intervals at each latitude and longitude gives 12×66 pairs of individual amplitudes at 66 time instances for 12 simulated SW events. Estimations of standard deviations of differences between these amplitude pairs and application of paired

Student t -test shows 95% statistical reliability of the differences between the mean amplitudes showed in Fig. 4, if the differences exceed 25, 5, 3, 2 g.p.m. for SPW1–SPW4, respectively.

Fig. 4 shows that in January–February SPWs have larger amplitudes in the Northern (winter) Hemisphere, than those in the Southern Hemisphere, because the background zonal circulation has eastward directions at all altitudes, which corresponds to waveguides for SPW propagation in winter (see Section 3.3). The left and middle panels of Fig. 4a show larger average SPW1 amplitude at altitudes 30–70 km at middle and high northern latitudes before and during SWs. In the mesosphere-lower thermosphere the SPW1 amplitude is increasing during SW (see Fig. 4a). Interactions of SPW1 with the mean eastward flow shown in Fig. 2a may contribute to decreases of the mean wind at high latitudes during SW.

Fig. 4b reveals that at altitudes 50–70 km at middle and high latitudes of the Northern Hemisphere, the amplitude maximum of SPW2 with $m = 2$ is largest before and become smaller during and after SWs. The SPW2 maxima in the stratosphere at altitudes 20–40 km in Fig. 4b is stronger during the composite SW event. Respectively, horizontal structures of temperature fields at altitude 30 km during simulated SWs in the left and middle panels of Fig. 3b have

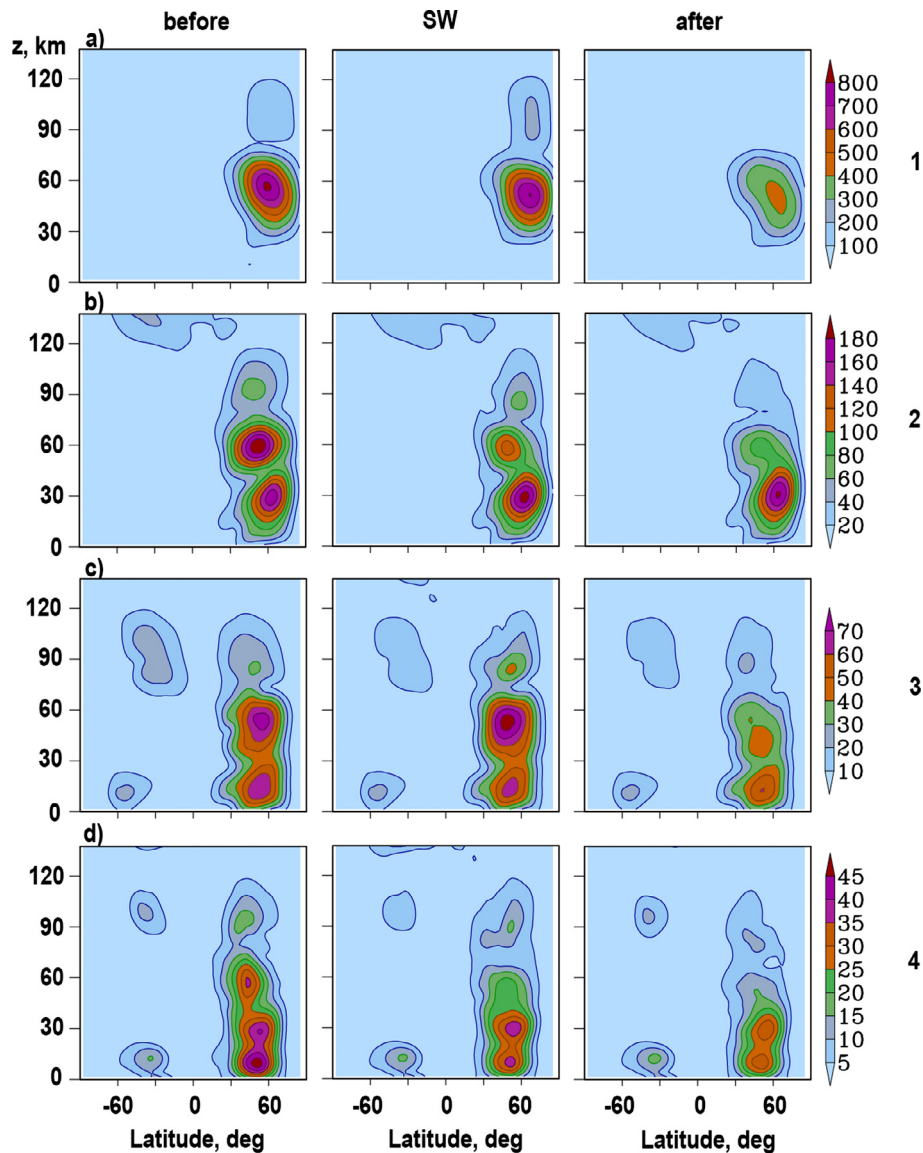


Fig. 4. Average amplitudes of geopotential (in gpm) variations caused by stationary planetary waves having zonal wave numbers $m = 1, 2, 3, 4$ (a, b, c, d), before (left), during (middle) and after (right) simulated composite SW event.

more pronounced temperature structures with two maxima and minima in longitude during SW. At altitude of 50 km, the left panel of Fig. 3a demonstrates two local maxima of the mean wind at high and middle latitudes before SW. During and after SW, the middle and right panels of Fig. 3a show decreases in the wind maxima at middle latitudes due to general slowdown of eastward winds. This corresponds to the decrease in SPW2 amplitude maximum at altitudes 50–70 km during and after SW in the middle and right panels of Fig. 4b. Numerical simulations by Robinson (1985) showed that relative variations of SPW1 and SPW2 amplitudes could be caused by nonlinear interactions between PW modes.

Fig. 4c and d shows larger SPW3 and SPW4 amplitudes in the Northern Hemisphere at altitudes 30–60 km and in the mesosphere – lower thermosphere at altitudes 80–

100 km and latitudes 30–60°N during and before simulated composite SW event, respectively. Right panels of Fig. 4 show general decrease in all SPW amplitudes after the SW, which may be caused by transformations of the background wind and temperature fields influencing SPW propagation conditions.

Fig. 5 depicts geopotential height amplitudes of NMs having different periods and propagating westward. Paired Student's t -test shows 95% statistical reliability of the differences between the mean amplitudes showed in Fig. 5, if the differences exceed 2, 10, 10, 10 g.p.m. for amplitudes of 4-, 5-, 7-, 10-day westward NMs, respectively. The main features of Fig. 5 are maxima of westward NM amplitudes existing not only in the Northern, but also in the Southern Hemisphere, where westward NMs can have waveguides for their propagation (e.g., Limpasuvan et al., 2016). Below

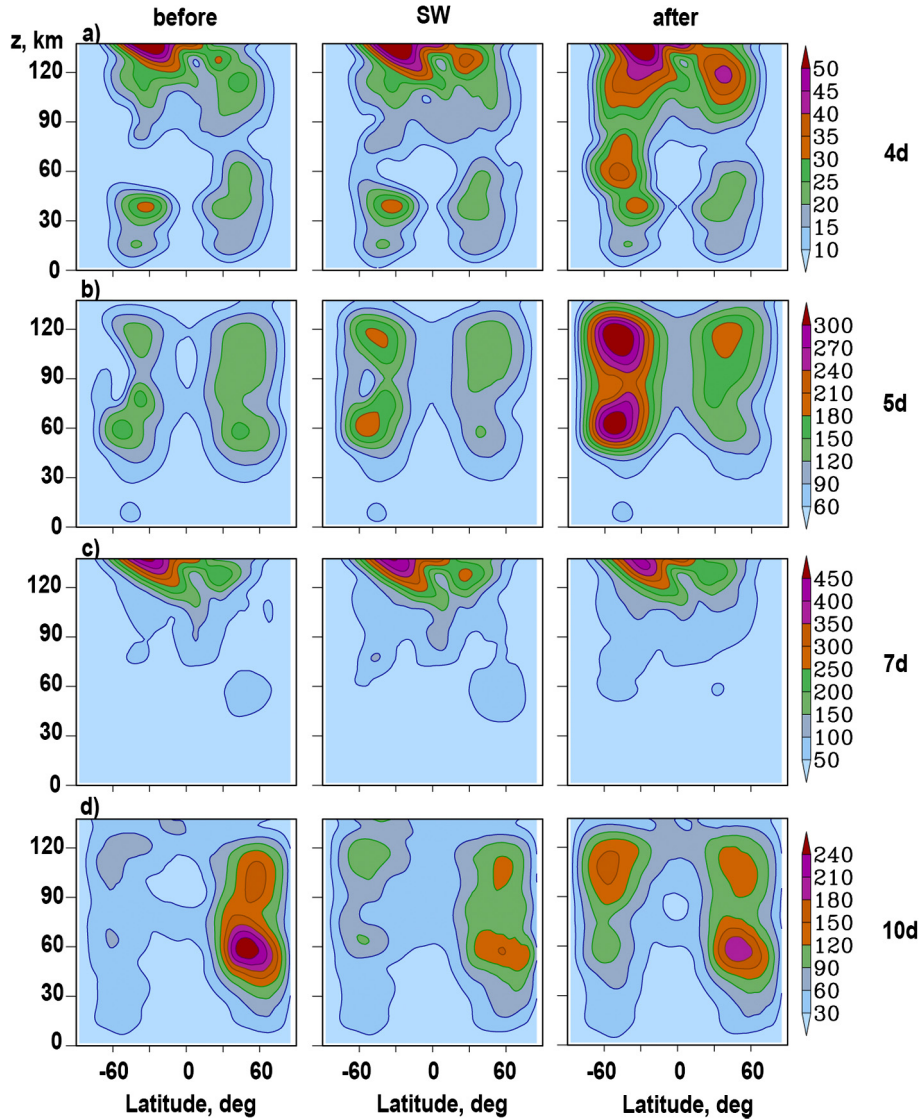


Fig. 5. Same as Fig. 4, but for westward travelling NMs with $\tau = 4$ d, $m = 2$ (a); $\tau = 5$ d, $m = 1$ (b); $\tau = 7$ d, $m = 2$ (c); $\tau = 10$ d, $m = 1$ (d).

altitudes of 100 km at the middle and high latitudes of the Northern Hemisphere, average amplitudes of all NMs except the 7-day mode are smaller during the composite SW than those before it (see Fig. 5).

Average amplitudes of westward NMs increase in the Southern Hemisphere after SW events in the right panels of Fig. 5. This may be associated with transformations of atmospheric general circulation seen in Figs. 2 and 3, which change PW EP-fluxes and refractive indices (see Section 3.3). In particular, significant temperature changes at high southern latitudes after SW seen in the right panel of Fig. 2b could be associated with increasing 5- and 10-day NMs having zonal wavenumber one. In the mesosphere – lower thermosphere at altitudes above 80–90 km, the 4- and 7-day NMs have largest amplitudes in the Southern Hemisphere, while amplitudes of the 5-day and 10-day NMs at the middle latitudes are largest in the Northern Hemisphere before SW and in the Southern Hemisphere after SW (see Fig. 5).

3.3. Refractive indices and Eliassen-Palm fluxes

Atmospheric regions, in which the background temperature and wind allow PW propagation, are known as the PW waveguides (Dickinson, 1968). Matsuno (1970) established the PW refractive index and showed that the best PW propagation exists in regions of positive index. To research the PW waveguide evolution during the SW, we employ the formula for the zonal-mean quasi-geostrophic refractive index squared, n_m^2 , for the wave mode having zonal wavenumber m (Karoly and Hoskins, 1982; Andrews et al., 1987):

$$n_m^2(\varphi, z) = \frac{q_\varphi}{\bar{u} - c} - \left(\frac{m}{a \cos \varphi} \right)^2 - \left(\frac{f}{2NH} \right)^2, \quad (1)$$

where q_φ is the latitudinal gradient of zonal-mean potential vorticity; \bar{u} is the zonal mean velocity of zonal wind; $c = 2\pi a \cos \varphi / (m\tau)$ is PW zonal phase speed; τ is PW per-

iod, z and φ are altitude and latitude; a is the radius of the Earth, f is the Coriolis parameter, N is the Brunt-Vaisala frequency, and H is the scale height for atmospheric pressure. For potential vorticity gradient q_φ in (1), we use conventional formulae (e.g., Eq. (2) given by Albers et al., 2013).

Another important characteristic of PW mode is the vector $\mathbf{F}_m = (F_m^{(\varphi)}, F_m^{(z)})$ of Eliassen-Palm flux (EP-flux). For log-pressure vertical coordinate and quasi-geostrophic conditions, the specific (divided by density) EP-flux components have the following forms (Andrews et al., 1987):

$$F_m^{(\varphi)} = -a \cos \varphi \overline{(u'v')}, \quad F_m^{(z)} = af \cos \varphi \overline{(v'\theta')}/\bar{\theta}_z, \quad (2)$$

where the primes denote perturbations produced by analyzed PW mode. Eq. (2) shows that an upward direction

of EP-flux vector corresponds to the northward wave heat flux; also southward EP-flux vector corresponds to the northward PW momentum flux. Gradients of n_m^2 can influence EP-flux vector (e.g. Albers et al., 2013). Therefore, the EP-flux vector and n_m^2 can be useful tools for analyzing the conditions of PW propagation in the latitude-altitude plane.

Simulated altitude-latitude regions of positive average $a^2 n_m^2$ for SPWs with $m = 1-4$ are plotted with shaded areas in Fig. 6. According to Eq. (1), at $c = 0$ the external boundaries of regions with positive n_m^2 are determined by critical levels, where $\bar{u} \rightarrow 0$ (which are the same for all SPWs) and by regions of high \bar{u} magnitudes (Charney and Drazin, 1961), when the first positive term at the right side of Eq. (1) becomes smaller than the sum of the rest negative terms. Eq. (1) gives $|n_m^2| \rightarrow \infty$ near the critical levels and $|n_m^2| \rightarrow 0$ at high \bar{u} magnitudes.

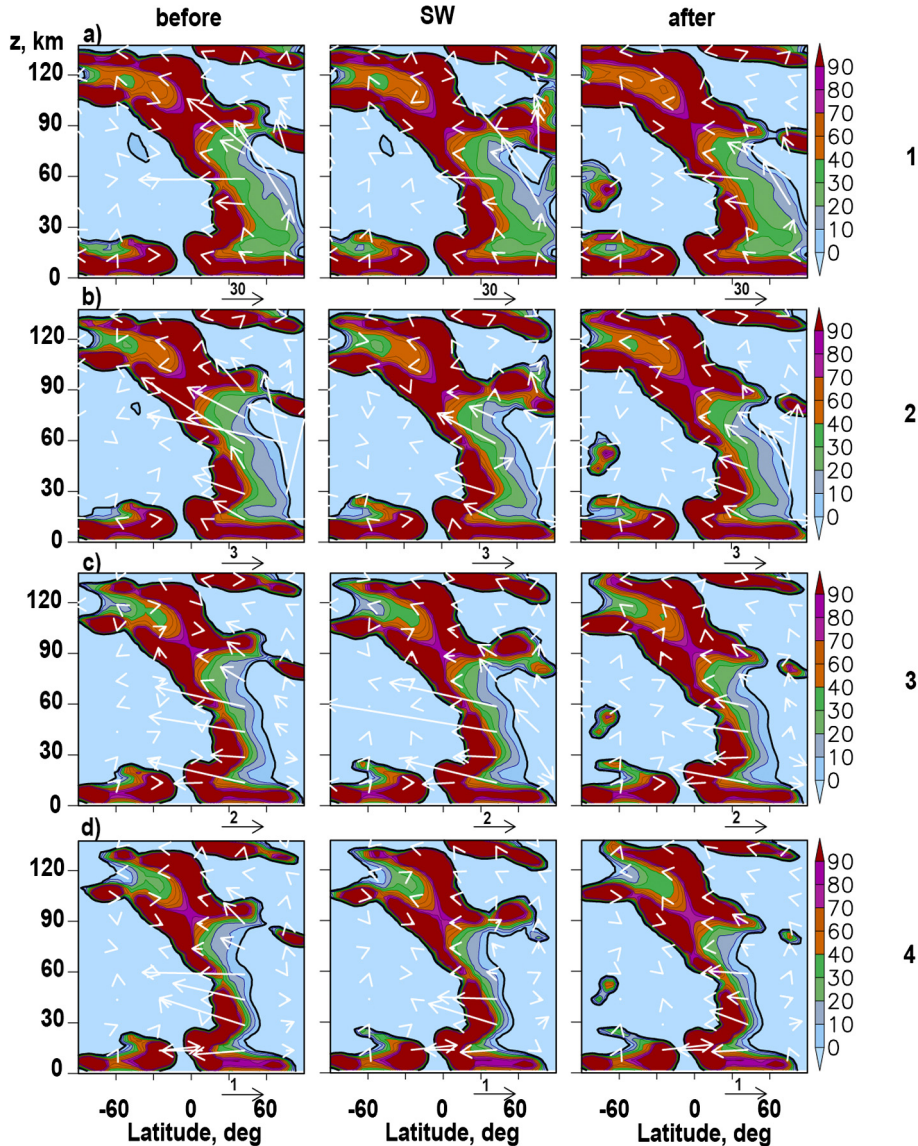


Fig. 6. Normalized refractive indices $a^2 n_m^2$ (shading) and specific EP fluxes in m^3/s^2 (arrows) produced by stationary planetary wave modes with zonal wavenumbers 1, 2, 3, 4 (panels a, b, c, d, respectively) averaged over time intervals before SW (left panels), and their changes during (middle panels) and after (right panels) SW averaged over 10 runs. Thick contours correspond to zero $a^2 n_m^2$.

Comparisons of the left panels of Fig. 6 with the left panel of Fig. 2a disclose PW waveguide locations in areas of eastward zonal-mean winds in both hemispheres. In the Northern Hemisphere at altitudes below 70 km, the waveguides with positive refractive index are bounded by the regions, where $\bar{u} \rightarrow 0$ and $a^2 n_m^2$ are very high in the south, and by the regions of high \bar{u} magnitudes in the north. The magnitude of the second negative term in the right side of Eq. (1) increases with m and SPW waveguides in Fig. 6 become more narrow at larger m . Above altitudes 50–60 km the waveguides in Fig. 6 cross the equator and allow SPW propagation into the mesosphere and thermosphere of the Southern Hemisphere.

Arrows in Fig. 6 reveal the specific EP-flux vectors given by Eq. (2). According to them, in Fig. 6a below altitudes 70–80 km the increased SPW propagation happens in the Northern (winter) Hemisphere at the middle latitudes, where EP-fluxes have upward directions at low altitudes and turn towards the equator at higher altitudes. This corresponds to existing studies of EP-fluxes in the stratosphere (e.g., Karoly and Hoskins, 1982; Smith, 2003; Inoue et al., 2011; Albers et al., 2013). Analysis of Fig. 6 reveals that SPW1 mode produces the strongest EP-fluxes in the northern middle atmosphere. Increasing m in the left panels of Fig. 6a–d leads to smaller magnitudes of EP-fluxes.

Middle and right panels of Fig. 6 depict simulated EP-flux vectors and $a^2 n_m^2$ for SPWs during and after SW. Changes in PW propagation conditions due to the changes of the zonal-mean winds shown in respective panels of Fig. 2a produce changes in $a^2 n_m^2$ and EP-flux vectors in Fig. 6. During SW in the middle panel of Fig. 6a, the northern boundary of the region of positive $a^2 n_m^2$ for SPW1 is shifted northward very close to the North Pole at altitudes 30–110 km compared to that before SW. This makes better conditions for SPW1 propagation during SW and could explain larger second maxima of SPW1 amplitudes at altitudes 70–100 km observed in the middle panel of Fig. 4a at latitudes 50–70° and higher EP-flux magnitudes there in the middle panel of Fig. 6a.

EP-fluxes for SPW1 have generally upward direction in the high-latitude strato-mesosphere in Fig. 6a, which corresponds to the northward wave heat flux (see Section 3.3). This leads to the heating of the respective high-latitude regions. Strengthening of SPW1 EP-flux at altitudes 50–70 km in the left panel of Fig. 6a could be one of the reasons of temperature maximum in the respective panel of Fig. 2b before SW near the North Pole. Possible heating of the high-latitude middle atmosphere by PWs and its variations due to stratospheric vacillations were previously discussed in literature (e.g., Holton and Mass, 1976; Pogoreltsev et al., 2014, 2015). Such wave heating could exist during SW also, but it can be masked by other heat sources in the middle panel of Fig. 2b.

For SPW2 in Fig. 6b, upward EP-fluxes in the middle latitudes of the Northern Hemisphere at altitudes above 50 km have larger magnitudes during SW. This corre-

sponds to larger SPW2 amplitudes at altitudes above 50 km in the left panel of Fig. 4b. For SPW3 and SPW4 in Fig. 6c and d, noticeable shifts of the northern boundary (up to 25–30° northward) of the region with $a^2 n_m^2 > 0$ during SW relative to that before SW occur at altitudes 90–100 km. This may explain stronger maximum of SPW3 amplitude in this region in the middle panel of Fig. 4c. Increases and decreases of magnitudes of EP-fluxes in Fig. 6c and d correspond to enhancements and weakening of SPW3 and SPW4 amplitude maxima in the Northern Hemisphere in Fig. 4c and d. Some long EP-flux vectors (especially in Fig. 6c) start in regions of negative $a^2 n_m^2$, which are not waveguides for SPW propagation. This may reflect wave generation in the middle atmosphere (for example due to nonlinear interactions of PW and the mean flow), which may be intensified during SW.

Fig. 7 shows EP-fluxes and $a^2 n_m^2$ for westward propagating NMs simulated including OGW parameterization into the MUAM. According to Eq. (1) for westward NMs having phase speeds $c < 0$, regions with $n_m^2 > 0$ can exist in the regions of westward zonal winds in the Southern (summer) Hemisphere. EP-flux vectors directed mainly southwards in Fig. 7 reveal that the westward propagating NMs can be mainly generated at middle and high latitudes of the Northern Hemisphere, from where they can propagate to the regions with $n_m^2 > 0$ in the Southern Hemisphere. Hence, amplitudes of westward NMs maximize in both hemispheres in Fig. 5. The largest areas with $n_m^2 > 0$ in Fig. 7 exist for 5- and 4-day NMs having largest magnitudes of westward phase speeds $c = -95 \text{ m s}^{-1}$ and $c = -61 \text{ m s}^{-1}$ at the equator, respectively. Thus, westward propagating short period NMs can provide dynamical links of both hemispheres in the middle and upper atmosphere. Considerations of Figs. 5 and 7 show substantial amplitudes and long EP-flux vectors for NM modes starting in regions of negative refractive index, where theory predicts poor conditions of PW propagation. This may reveal PW energy tunneling and wave generation in these areas (for example, due to nonlinear interactions of PW and the mean flow).

EP-fluxes produced by 4- and 7-day NMs with $m = 2$ have large magnitudes and mainly southward directions at altitudes above 100 km in Fig. 7a and c. They partly started at northern high latitudes in the regions with $n_m^2 < 0$, where local sources in the upper atmosphere and wave energy tunneling from below can contribute to NM generation. Southward EP-fluxes for 4-day and 7-day NMs exist at almost all latitudes in the lower thermosphere in Fig. 7a and c. Divergence of these EP-fluxes produces strong maxima of 4-day and 7-day NMs at altitudes above 100 km at middle latitudes of the Southern Hemisphere in Fig. 5a and c. During SW, magnitudes of the EP-fluxes in the thermosphere change in the Northern hemisphere in Fig. 7a and c, which may cause changes in the respective EP-fluxes and 4-day and 7-day NM amplitudes in Fig. 5a and c in the Southern Hemisphere.

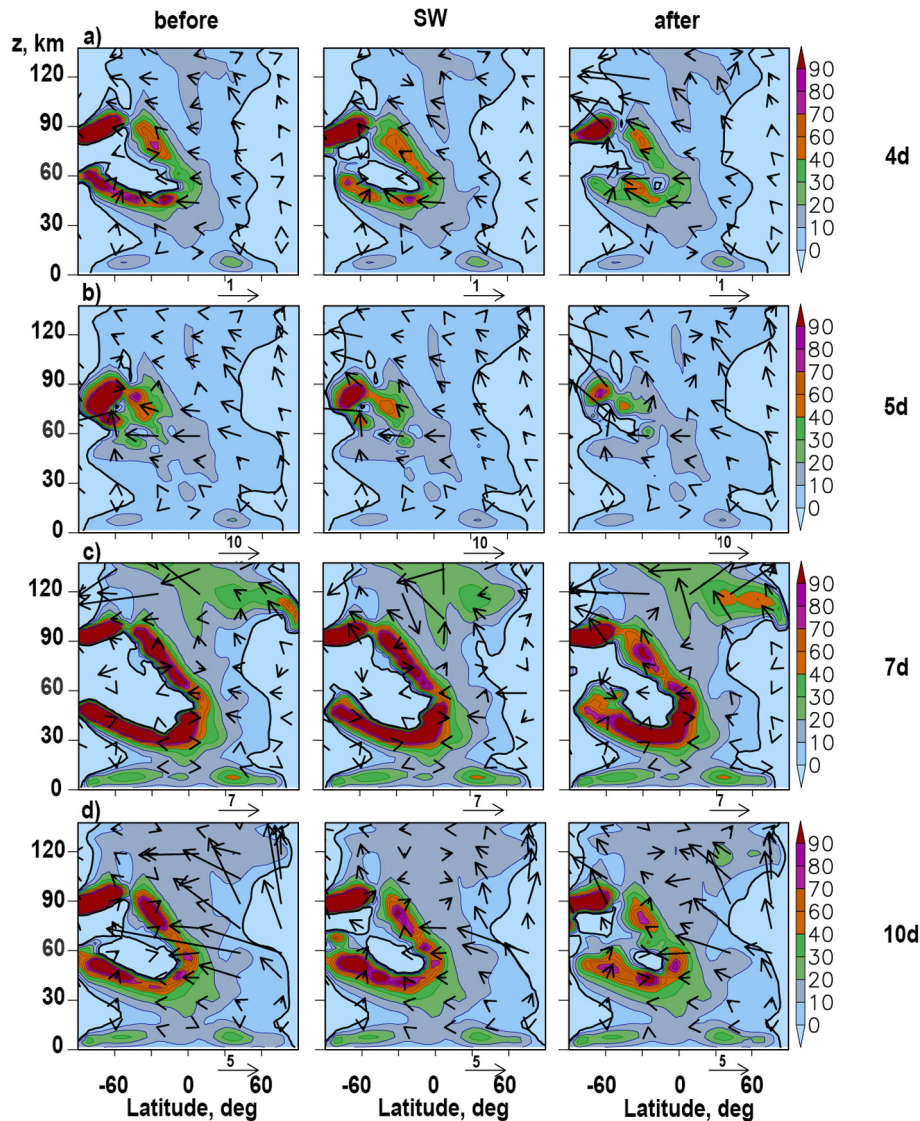


Fig. 7. Same as Fig. 6, but for westward travelling NMs with $\tau = 4$ d, $m = 2$ (a); $\tau = 5$ d, $m = 1$ (b); $\tau = 7$ d, $m = 2$ (c); $\tau = 10$ d, $m = 1$ (d).

The second region of increased southward EP-fluxes of 4-day and 7-day NMs exists at altitudes 30–70 km in Fig. 7a and c. These fluxes can contribute to the formation of NM amplitude maxima at altitudes 30–70 km at middle latitudes of the Southern Hemisphere observed in Fig. 5a and c. These maxima are more noticeable in Fig. 5a due to more extended waveguides with $n_m^2 > 0$ in the Southern Hemisphere for 4-day NM (see above).

For 5-day and 10-day NMs having $m = 1$, southward EP-fluxes in the lower thermosphere are smaller than those at altitudes 40–70 km in Fig. 7b and d. Respectively, amplitude maxima in Fig. 5b and d in the thermosphere are smaller and are located at lower altitudes than those for 4-day and 7-day NMs. Amplitude maxima in the stratosphere of the Southern Hemisphere are largest for 5-day NMs in Fig. 5b, which has largest magnitude of westward phase speed and largest areas of waveguide with $n_m^2 > 0$ in Fig. 7. Modulation of NM southward EP-fluxes by SW seen in Fig. 7 may produce modulation of

respective NM amplitudes in the Southern Hemisphere observed in Fig. 5.

Vertical EP-flux components in Fig. 7 are generally positive in the middle atmosphere at middle and high latitudes of the Northern Hemisphere. In accordance with Eq. (2), this matches to northward wave heat fluxes and additional heating by NMs in areas near the North Pole. Figs. 6 and 7 reveal that variations of PW and NM amplitudes presented in Figs. 4 and 5 may be associated with changes in the mean temperature and wind, EP-fluxes and PW refractive index for time intervals before, during and after the SW events.

3.4. Influence of stationary orographic gravity waves

Described above simulations were made including the parameterization of OGW dynamical and heating effects into the MUAM. In this section, we estimated OGW contribution. First, we made the same simulations and gener-

ated 12-member ensemble of runs, but without OGW parameterization in the MUAM (see Section 3). Comparing 6 of 12 pairs of the MUAM runs, for which the correspondence of SWs with and without OGW was clear, we found that inclusion of OGW effects leads to 15–25 day shift to earlier dates of simulated SWs. For comparisons we calculated differences of PW amplitudes between MUAM runs including and excluding OGW parameterization averaged over 11-day time intervals before, during and after respective SW events. Positive and negative differences correspond, respectively, to increases and decreases in PW amplitudes due to inclusion of OGW effects.

Fig. 8 shows increments of geopotential height amplitude for SPW1–SPW4. To confirm statistical significance of nonzero SPW amplitude increments in Fig. 8, we used

the paired Student’s *t*-test (Rice, 2006). From 12 MUAM runs excluding and including the OGW parameterization for the comparison at each altitude and latitude for every 11-day interval, we obtained 12×66 pairs of SPW amplitudes in 66 time moments (4-hour outputs) and 12 SW events. The paired Student’s *t*-tests give 95% statistical confidence of nonzero SPW amplitude differences inside regions marked with dashed lines in Fig. 8.

In Fig. 8a, we observe general increases (up to 15%) of average SPW1 amplitudes at altitudes 40–70 km at middle and high latitudes of the Northern Hemisphere caused by OGW effects during SW and decreases before and after the event. In Fig. 8b, OGW inclusion leads to increases of SPW2 maxima shown in Fig. 4b below 50 km and decreases above this altitude. However, during SWs, one

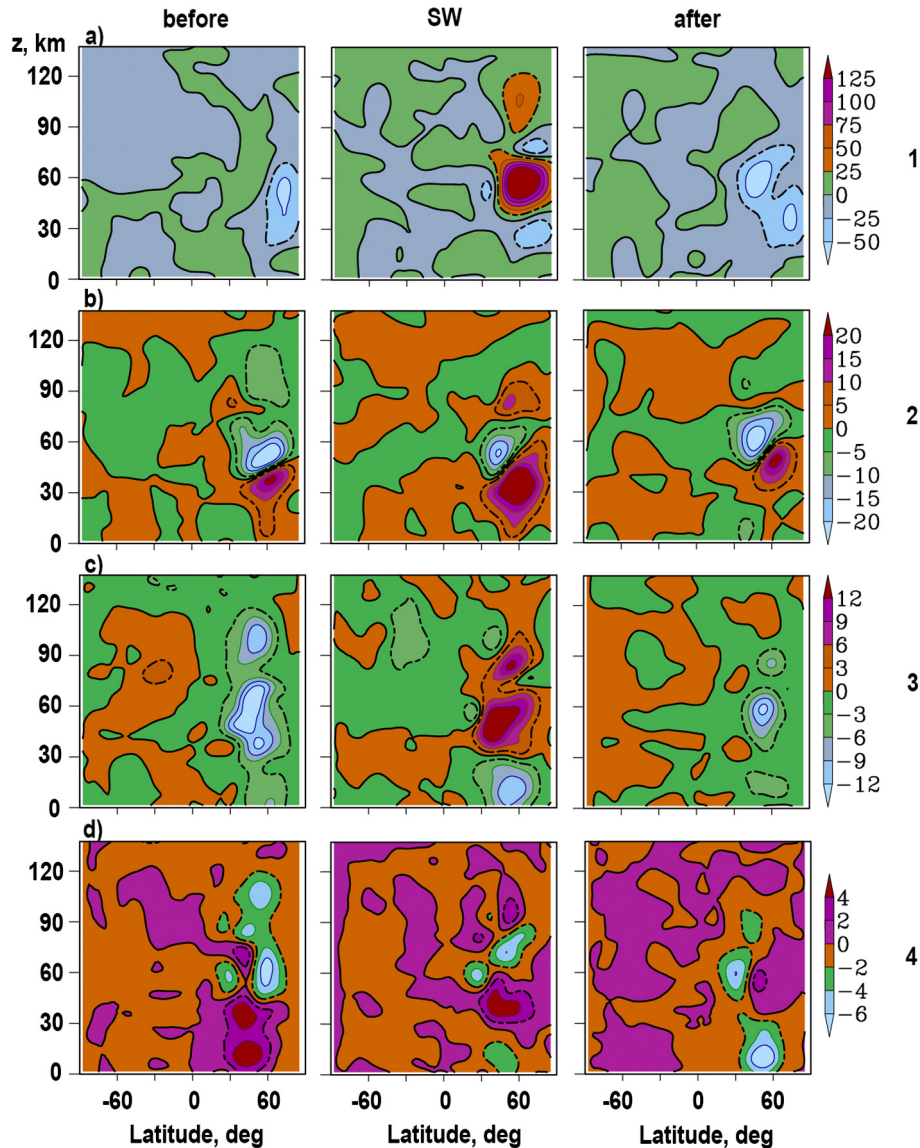


Fig. 8. Average differences of geopotential amplitudes of stationary planetary waves with $m = 1, 2, 3, 4$ (a, b, c, d) caused by OGW effects before (left), during (middle) and after (right) simulated composite SW event. Thick contours show zero values. Dashed contours denote boundaries of regions with 95% statistical confidence.

can see enhancement of these increments up to 15%. Therefore, OGW influence could contribute to weakening of the mesospheric SPW2 maximum during SW seen in the middle panel of Fig. 4b. The SPW3 amplitudes at the middle and high latitudes of the Northern Hemisphere in Fig. 8c are generally decreasing due to OGW influence before SW and increasing during SW, contributing to the SPW3 amplitude increase during SW in the middle panel of Fig. 4c. After SW, negative changes (up to -20%) of SPW3 and SPW4 amplitudes caused by OGW effects dominate at altitudes below 60 km at the middle and high latitudes of the Northern Hemisphere in the right panels of Fig. 8c and d.

One of the mechanisms of direct impacts of gravity waves on amplitudes of PW modes could be wave drag of the mean flow (e.g., McLandress and McFarlane, 1993; Smith, 2003). In Fig. 3c, we plotted horizontal distributions of OGW amplitudes at altitude 50 km during different SW phases. Similar distributions have zonal and meridional components of the mean wind drag by OGWs (Gavrilov and Koval, 2013). It is possible to obtain Fourier components of zonal and meridional OGW drag versus longitude (examples are given by Gavrilov et al., 2015). It is essential that zonal and meridional OGW drag components at high latitudes could influence, respectively, meridional and zonal components of atmospheric general circulation and SPWs.

Depending on phase shifts between Fourier components of OGW drag, PWs and atmospheric circulation, direct impacts of OGW drag can lead to local increases or decreases in SPW amplitudes. The phase shifts may vary almost randomly due to wind variability in the mountain systems and changes in conditions of SPW and OGW propagation at different latitudes and altitudes. Therefore, direct impacts of OGW drag could lead to variable local increases and decreases of SPW amplitudes in different regions of the atmosphere.

Fig. 2c shows that described direct impacts of OGW drag in January–February may primarily occur at middle latitudes of the Northern Hemisphere at altitudes up to 80 km. Modified SPW modes may then propagate out of this zone, interact with the mean circulation, and thus expand this indirect OGW impact to other latitudes and altitudes, including the Southern Hemisphere, as it is shown in Fig. 8. For example, possible role of nonlinear PW-mean flow interactions in expansions of low-latitude perturbations at low altitudes during QBO to the mid-latitude middle atmosphere was widely illustrated (e.g., Holton and Tan, 1980; Pascoe et al., 2005; Inoue et al., 2011; Yamashita et al., 2011; Watson and Gray, 2014). Previously, we noted in Fig. 3c the dominance of OGWs generated by the North American and European mountain systems before and during SW, and the dominance of OGWs from Himalayas after SW. This could change horizontal distributions of OGW drag in the middle atmosphere and produce different OGW influence on SPW amplitudes in different stages of SWs.

Fig. 9 shows differences in amplitudes of westward propagating NMs caused by inclusion of OGW parameterization into the MUAM model. The left panels of Fig. 9 reveal that before SW, the main OGW effects are generally located above 60 km for all NMs. Changes of NM amplitudes can reach up to 10–50%. The amplitude of 10-day NM amplitude increases at middle and high northern latitudes in the left panel of Fig. 9d. During SW, the middle panels of Fig. 9a–c show substantial increases and decreases in amplitudes of westward NMs in the Southern Hemisphere at altitudes above 60 km, and their general decreases at high latitudes of the Northern Hemisphere. The middle panel of Fig. 9d demonstrates increases in the amplitude of 10-day NAM in both hemispheres above altitudes 50–60 km. After SW, the right panels of Fig. 9 depict generally positive amplitude changes in the Southern Hemisphere above altitudes 30–40 km caused by OGW impacts.

For better estimating OGW influence, we calculated differences in EP-fluxes and refractive indices between MUAM calculations including and excluding parameterization of OGW dynamical and thermal effects for simulated SPW and NM modes before, during and after the composite SW events. Positive and negative $a^2 n_m^2$ increments as well as southward and northward directed EP-flux increments correspond in most cases to increasing and decreasing in SPW and NM amplitudes that confirms PW theory.

Simulations in this study used only one set of climatological data corresponding to 20-year average January–February conditions. Results obtained above show that the influence of OGW and PW drag could give different effects in different SW stages and for different SPWs and NMs. Therefore, further numerical experiments are required for other climatological conditions. OGW drag can both increase and decrease amplitudes of different PW and NM modes in different SW stages.

In the present study, we analyzed the impact of OGWs only. An important contribution to PW and general circulation variations can give, for example, varying heating during the tropospheric storm passages (Valdes and Hoskins, 1989; Hoskins and Valdes, 1990). It would be helpful to study separate influences of OGW effects and other contributions separately for each SW instance for better understanding their joint influences.

4. Summary and conclusion

Numerical simulations of the planetary wave propagation into the middle and upper atmosphere during SW events were performed with the mechanistic MUAM general circulation model. Parameterization schemes of NMs and OGWs have been implemented into MUAM. Based on the 12-runs ensemble with this model a composite SW event using the UK Met Office lower boundary conditions averaged over January–February 1992–2011 were con-

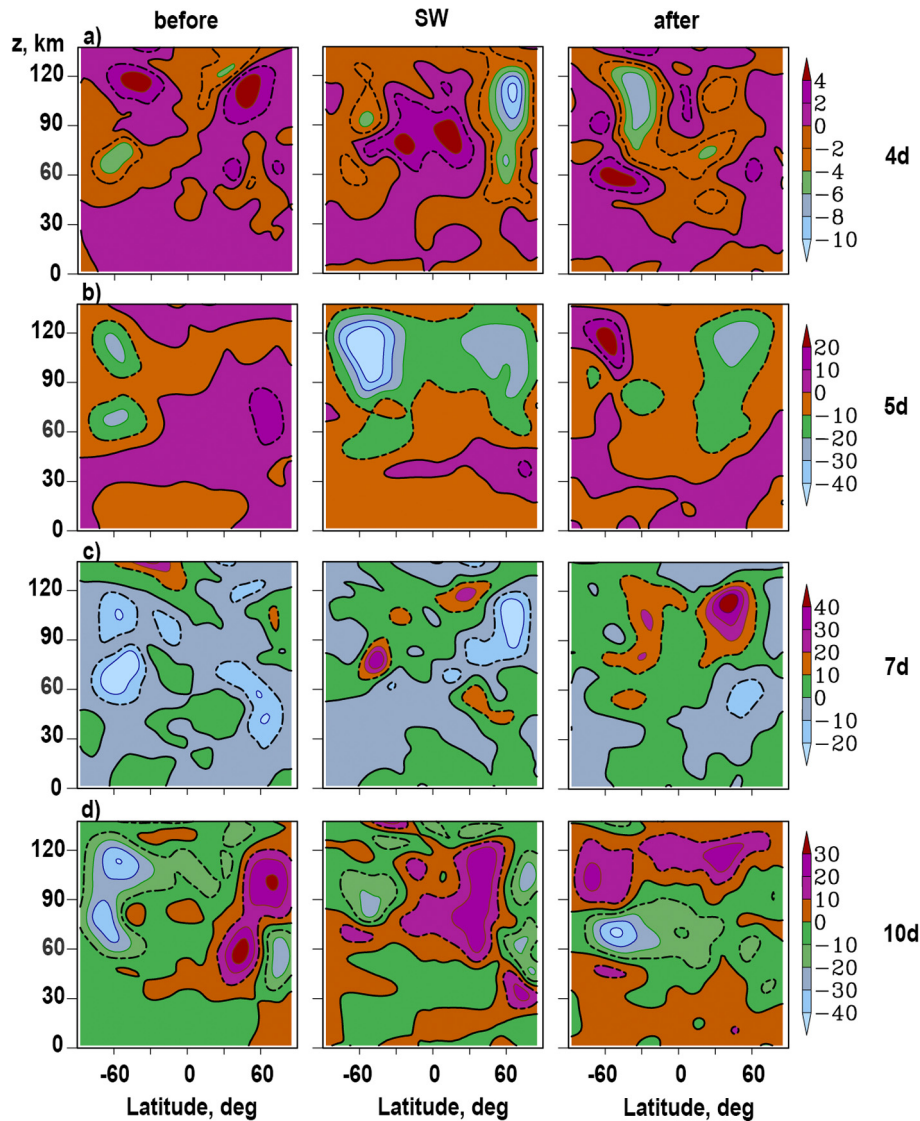


Fig. 9. Same as Fig. 8, but for westward travelling NMs with $\tau = 4$ d, $m = 2$ (a); $\tau = 5$ d, $m = 1$ (b); $\tau = 7$ d, $m = 2$ (c); $\tau = 10$ d, $m = 1$ (d).

structured. The results of simulations show the existence of SWs, which are very similar to these events observed in different years. The amplitudes of stationary PW modes and westward travelling NMs with January–February climatological conditions were analyzed for time intervals before, during, and after the composite SW event. Twelve pairs of runs were conducted with and without inclusion of the parameterization of OGW dynamical and thermal effects.

Comparison of composites obtained by averaging over twelve simulated SW events with and without OGW parameterization allows us to make the following conclusion. Simulations demonstrate substantial variations of amplitudes of SPWs during and after the SW at high latitudes of the Northern Hemisphere. Average SPW1 amplitude at altitudes 30–70 km at middle and high northern latitudes are larger before and during SWs. In the mesosphere-lower thermosphere, the SPW1 amplitude is increasing during SW. Interactions of SPW1 with the mean eastward flow may contribute to reverses of the mean wind

at high latitudes during SW. At altitudes 50–100 km at high latitudes of the Northern Hemisphere, the amplitude maximum of SPW2 with $m = 2$ is largest before and become smaller during and after SWs. The SPW2 maxima in the stratosphere at altitudes 20–40 km are stronger during the composite SW event. SPW3 amplitudes in the Northern Hemisphere at altitudes 30–100 km are larger during simulated SW events. SPW4 amplitudes decrease during the composite SW. SPW amplitudes are up to 20–40% smaller after the SW. In general, the enhancements of SPW1–SPW3 below 50 km as well as weakening SPW2 and SPW4 above altitudes 50 km at middle and high latitudes in the Northern Hemisphere are observed in runs including OGW parameterization during SW.

Westward travelling NMs have amplitude maxima not only in the Northern, but also in the Southern Hemisphere, where these modes are capable of propagating through stratospheric waveguides (e.g., Limpasuvan et al., 2016). Largest amplitudes in the Southern Hemisphere have 5-

day NM in the strato-mesosphere and 4-day and 7-day NMs in the lower thermosphere. Below altitudes 70–80 km at the middle and high latitudes of the Northern Hemisphere, average amplitudes of all NMs are smaller during composite SW than those before it. Average amplitudes of westward NMs increase in the Southern Hemisphere after SW. Simulated variations of SPW and NM amplitudes correspond to changes in the mean zonal wind, EP-fluxes and PW refractive index in the time intervals before, during and after the SW events. Thus, westward travelling NMs can transport wave momentum and wave activity from the winter to summer hemisphere. SW events in the winter hemisphere can modulate meridional Eliassen-Palm fluxes and change NM amplitudes in the summer hemisphere.

Inclusion of the parameterization of OGW dynamical and thermal effects leads to 15–25 day shift to earlier dates of simulated SWs. The changes in SPW amplitudes generally correspond to variations of n_m^2 and EP-flux magnitudes caused by the OGW effects.

The main effects of the inclusion of OGW parameterization into the MUAM model are substantial changes in amplitudes of westward propagating NMs at middle and high latitudes of the Southern Hemisphere, and decreases of 4- and 5-day NMs in the Northern Hemisphere during SW. After SW, OGW impacts produce generally positive amplitude changes in the Southern Hemisphere above altitudes 30–40 km. The observed changes in NM amplitudes in the Southern Hemisphere during SW can be explained by divergence of increased southward EP-flux. The EP-flux can increase due to OGW drag before SW, and extends into the Southern Hemisphere. Further numerical experiments are required for other initial and climatological conditions.

Acknowledgements

The authors are grateful to the British Atmospheric Data Centre for providing access to the UK Met Office meteorological data for SW analysis. The improvements of OGW parameterization were supported by the Russian Basic Research Foundation (#16-35-60013mol_a_dk). Numerical simulations and their interpreting were supported by the Russian Science Foundation (#14-17-00685).

References

Albers, J.R., McCormack, J.P., Nathan, T.R., 2013. Stratospheric ozone and the morphology of the Northern Hemisphere planetary waveguide. *J. Geophys. Res. Atmos.* 118, 563–576. <http://dx.doi.org/10.1029/2012JD017937>.

Andrews, D.G., Holton, J.R., Leovy, C.B., 1987. *Middle Atmosphere Dynamics*. Elsevier, New York.

Bittner, M., Offermann, D., Graef, H.H., 2000. Mesopause temperature variability above a midlatitude station in Europe. *J. Geophys. Res.* 105 (D2), 2045–2058.

Buhler, O., 2009. *Waves and Mean Flows*. Cambridge University Press, New York, p. 341.

Buriti, R.A., Takahashi, H., Lima, L.M., Medeiros, A.F., 2005. Equatorial planetary waves in the mesosphere observed by airglow periodic oscillations. *Adv. Space Res.* 35, 2031–2036.

Butler, A., Seidel, D., Hardiman, S., et al., 2015. Defining sudden stratospheric warmings. *Bull. Amer. Meteorol. Soc.* 96, 1913–1928. <http://dx.doi.org/10.1175/BAMS-D-13-00173.1>.

Catry, B., Geleyn, J.F., Bouysse, F., Cedilnik, J., Broo, R., Derková, M., Mladek, R., 2008. A new sub-grid scale lift formulation in a mountain drag parameterisation scheme. *Meteorol. Zeitschrift* 17 (2), 193–208.

Charlton, A.J., Polvani, L.M., 2007. A new look at stratospheric sudden warmings. Part I: Climatology and modeling benchmarks. *J. Clim.* 20, 449–469.

Charney, J.G., Drazin, P.G., 1961. Propagation of planetary-scale disturbances from the lower into the upper atmosphere. *J. Geophys. Res.* 66, 83–109.

Cohen, N., Gerber, E.P., Buhler, O., 2013. Compensation between resolved and unresolved wave driving in the stratosphere: implications for downward control. *J. Atmos. Sci.* 70, 3780–3798.

Cohen, N., Gerber, E.P., Buhler, O., 2014. What drives the Brewer-Dobson circulation. *J. Atmos. Sci.* 71 (10), 3837–3855.

Dickinson, R.E., 1968. Planetary Rossby waves propagating vertically through weak westerly wave guides. *J. Atmos. Sci.* 25, 984–1002.

Ebel, A., Berger, U., Krueger, B.C., 1995. Numerical simulations with COMMA, a global model of the middle atmosphere. *SIMPO Newsletter*, 12, 22–32.

Espy, P.J., Stegman, J., Witt, G., 1997. Interannual variations of the quasi-16-day oscillation in the polar summer mesospheric temperature. *J. Geophys. Res.* 102, 1983–1990.

Fagundes, P.R., Goncharenko, L.P., de Abreu, A.J., Venkatesh, K., et al., 2015. Ionospheric response to the 2009 sudden stratospheric warming over the equatorial, low, and middle latitudes in the South American sector. *J. Geophys. Res. Space Phys.* 120 (9), 7889–7902.

Fedulina, I.N., Pogoreltsev, A.I., Vaughan, G., 2004. Seasonal, interannual and short-term variability of planetary waves in UKMO assimilated fields. *Quart. J. Roy. Meteorol. Soc.* 130 (602), 2445–2458.

French, W.J.R., Burns, G.B., 2004. The influence of large-scale oscillations on long-term trend assessment in hydroxyl temperatures over Davis, Antarctica. *J. Atmos. Sol.-Terr. Phys.* 66 (6–9), 493–506.

Fuller-Rowell, T., Wu, F., Akmaev, R., Fang, T.-W., Araujo-Pradere, E., 2010. A whole atmosphere model simulation of the impact of a sudden stratospheric warming on thermosphere dynamics and electrodynamics. *J. Geophys. Res.* 115, A00G08. <http://dx.doi.org/10.1029/2010JA015524>.

Funke, B., Lopez-Puertas, M., Bermejo-Pantaleon, D., Garcia-Comas, M., Stiller, G.P., von Clarmann, T., Kiefer, M., Linden, A., 2010. Evidence for dynamical coupling from the lower atmosphere to the thermosphere during a major stratospheric warming. *Geophys. Res. Lett.* 37, L13803. <http://dx.doi.org/10.1029/2010GL043619>.

Gavrilov, N.M., Koval, A.V., 2013. Parameterization of mesoscale stationary orographic wave impact for usage in numerical models of atmospheric dynamics. *Izvestia Atmos. Ocean. Phys.* 49 (3), 243–251.

Gavrilov, N.M., Pogoreltsev, A.I., Jacobi, Ch., 2005. Numerical modeling of the effect of latitude-inhomogeneous gravity waves on the circulation of the middle atmosphere. *Izvestia Atmos. Ocean. Phys.* 41 (1), 9–18.

Gavrilov, N.M., Koval, A.V., Pogoreltsev, A.I., Savenkova, E.N., 2013a. Numerical simulation of the response of general circulation of the middle atmosphere to spatial inhomogeneities of orographic waves. *Izvestiya Atmos. Ocean. Phys.* 49 (4), 367–374.

Gavrilov, N.M., Koval, A.V., Pogoreltsev, A.I., Savenkova, E.N., 2013b. Numerical modeling influence of inhomogeneous orographic waves on planetary waves in the middle atmosphere. *Adv. Space Res.* 51 (11), 2145–2154.

Gavrilov, N.M., Koval, A.V., Pogoreltsev, A.I., Savenkova, E.N., 2015. Simulating influences of QBO phases and orographic gravity wave forcing on planetary waves in the middle atmosphere. *Earth Planets Space* 67, 86. <http://dx.doi.org/10.1186/s40623-015-0259-2>.

- Geller, M.A., Zhou, T., Ruedy, R., 2011. New gravity wave treatments for GISS climate models. *J. Clim.* 24, 3989–4002. <http://dx.doi.org/10.1175/2011JCLI4013.1>.
- Goncharenko, L., Coster, A., Plumb, R., Domeisen, D., 2012. The potential role of stratospheric ozone in the stratosphere-ionosphere coupling during stratospheric warmings. *Geophys. Res. Lett.* 39, L08101. <http://dx.doi.org/10.1029/2012GL051261>.
- Gossard, E.E., Hooke, W.H., 1975. *Waves in the Atmosphere*. Elsevier Sci. Publ. Co., Amsterdam-Oxford-New York.
- Hedin, A.E., Fleming, E.L., Manson, A.H., Schmidlin, F.J., Avery, S.K., Clark, R.R., Franke, S.J., Fraser, G.J., Tsuda, T., Vial, F., Vincent, R. A., 1996. Empirical wind model for the upper, middle and lower atmosphere. *J. Atmos. Terr. Phys.* 58, 1421–1447.
- Hoffmann, P., Jacobi, Ch., Borries, C., 2012. A possible planetary wave coupling between the stratosphere and ionosphere by gravity wave modulation. *J. Atmos. Sol.-Terr. Phys.* 75–76, 71–80. <http://dx.doi.org/10.1016/j.jastp.2011.07.008>.
- Holton, J.R., 1975. The dynamic meteorology of the stratosphere and mesosphere. *Meteorol. Monogr.* 15 (37), 1–218.
- Holton, J.R., 1984. The generation of mesospheric planetary waves by zonally asymmetric gravity wave breaking. *J. Atmos. Sci.* 41 (23), 3427–3430.
- Holton, J.R., Mass, C., 1976. Stratospheric vacillation cycles. *J. Atmos. Sci.* 33, 2218–2215.
- Holton, J., Tan, H., 1980. The influence of the equatorial quasi-biennial oscillation on the global circulation at 50 mb. *J. Atmos. Sci.* 37, 2200–2208.
- Hoskins, B.J., Valdes, P.J., 1990. On the existence of storm-tracks. *J. Atmos. Sci.* 47 (15), 1854–1864.
- Inoue, M., Takahashi, M., Naoe, H., 2011. Relationship between the stratospheric quasi-biennial oscillation and tropospheric circulation in northern autumn. *J. Geophys. Res.* 116, D24115. <http://dx.doi.org/10.1029/2011JD016040>.
- Jacobi, Ch., Fröhlich, K., Portnyagin, Y., 2009. Semi-empirical model of middle atmosphere wind from the ground to the lower thermosphere. *Adv. Space Res.* 43, 239–246.
- Miyahara, S., Hayashi, Y., Mahlman, J.D., 1986. Interactions between gravity waves and planetary-scale flow simulated by the GFDL “SKYHI” general circulation model. *J. Atmos. Sci.* 43 (17), 1844–1861.
- Karoly, D.J., Hoskins, B.J., 1982. Three dimensional propagation of planetary waves. *J. Meteor. Soc. Jpn.* 60, 109–123.
- Kim, Y.J., Arakawa, A., 1995. Improvement of orographic gravity wave parameterization using a mesoscale gravity wave model. *J. Atmos. Sci.* 52 (11), 1875–1902.
- Kurihara, J., Ogawa, Y., Oyama, S., Nozawa, S., Tsutsumi, M., Hall, C. M., Tomikawa, Y., Fujii, R., 2010. Links between a stratospheric sudden warming and thermal structures and dynamics in the high-latitude mesosphere, lower thermosphere, and ionosphere. *Geophys. Res. Lett.* 37 (L13806), 2010. <http://dx.doi.org/10.1029/2010GL043643>.
- Kuttippurath, J., Nikulin, G., 2012. The sudden stratospheric warming of the Arctic winter 2009/2010: comparison to other recent warm winters. *Atmos. Chem. Phys. Discuss.* 12, 7243–7271.
- Labitzke, K., 1977. Interannual variability of the winter stratosphere in the Northern Hemisphere. *Mon. Weather Rev.* 105, 762–770. [http://dx.doi.org/10.1175/1520-0493\(1977\)105<0762:IVOTWS>2.0.CO;2](http://dx.doi.org/10.1175/1520-0493(1977)105<0762:IVOTWS>2.0.CO;2).
- Labitzke, K., Kunze, M., 2009. On the remarkable Arctic winter in 2008/2009. *J. Geophys. Res.* 114, D00102. <http://dx.doi.org/10.1029/2009JD012273>.
- Labitzke, K., Naujokat, B., Kunze, M., 2005. The lower Arctic stratosphere in winter since 1952: an update. *SPARC Newslett.* 24, 27–28.
- Limpasuvan, V., Orsolini, Y.J., Chandran, A., Garcia, R.R., Smith, A.K., 2016. On the composite response of the MLT to major sudden stratospheric warming events with elevated stratopause. *J. Geophys. Res.* Atmos. 121, 4518–4537. <http://dx.doi.org/10.1002/2015JD024401>.
- Liu, H., Doornbos, E., Yamamoto, M., Ram, S.T., 2011. Strong thermospheric cooling during the 2009 major stratosphere warming. *Geophys. Res. Lett.* 38, L12102. <http://dx.doi.org/10.1029/2011GL047898>.
- Longuet-Higgins, M.S., 1968. The eigenfunctions of Laplace’s tidal equation over a sphere. *Philos. Trans. Roy. Soc. Lond.* 262, 511–607.
- López-González, M.J., Rodríguez, E., García-Comas, M., Costa, V., Shepherd, M.G., Shepherd, G.G., Aushev, V.M., Sargoytchev, S., 2009. Climatology of planetary wave type oscillations with periods of 2–20 days derived from O2 atmospheric and OH(6–2) airglow observations at midlatitude with SATI. *Ann. Geophys.* 27, 3645–3662.
- Lott, F., Miller, M.J., 1997. A new subgrid-scale orographic drag parametrization: its formulation and testing. *Quart. J. Roy. Meteorol. Soc.* 123, 101–127.
- Matsuno, T., 1970. Vertical propagation of stationary planetary waves in the winter Northern Hemisphere. *J. Atmos. Sci.* 27, 871–883.
- Mayr, H.G., Mengel, J.G., Chan, K.L., Huang, F.T., 2011. Middle atmosphere dynamics with gravity wave interactions in the numerical spectral model: tides and planetary waves. *J. Atmos. Sol.-Terr. Phys.* 73, 711–730.
- McInturf, R.M., 1978. Stratospheric warmings: Synoptic, dynamic, and general circulation aspects. *NASA Ref. Publ.* 1017, 166pp.
- McIntyre, M.E., 1982. How well do we understand the dynamics of stratospheric warmings. *J. Meteorol. Soc. Jpn.* 60, 37–64.
- McLandress, C., 2002. The seasonal variation of the propagating diurnal tide in the mesosphere and lower thermosphere. Part I: The role of gravity waves and planetary waves. *J. Atmos. Sci.* 59, 893–906.
- McLandress, C., McFarlane, N.A., 1993. Interactions between orographic gravity wave drag and forced stationary planetary waves in the winter Northern Hemisphere middle atmosphere. *J. Atmos. Sci.* 50 (13), 1966–1990. [http://dx.doi.org/10.1175/1520-0469\(1993\)050<1966:IBOGWD>2.0.CO;2](http://dx.doi.org/10.1175/1520-0469(1993)050<1966:IBOGWD>2.0.CO;2).
- McLandress, C., Shepherd, T.G., Polavarapu, S., Beagly, S., 2012. Is missing orographic gravity wave drag near 60S the cause of the stratospheric zonal wind biases in chemistry–climate models?. *J. Atmos. Sci.* 69, 802–818.
- Murphy, D.J., French, W.J.R., Vincent, R.A., 2007. Long-period planetary waves in the mesosphere and lower thermosphere above Davis, Antarctica. *J. Atmos. Sol.-Terr. Phys.* 69 (17–18), 2118–2138.
- Nath, D., Chen, W., Zelin, C., Pogoreltsev, A.I., Wei, K., 2016. Dynamics of 2013 sudden stratospheric warming event and its impact on cold weather over Eurasia: role of planetary wave reflection. *Sci. Rep.* 6, 24174. <http://dx.doi.org/10.1038/srep24174>.
- Ortland, D.A., Alexander, M.J., 2006. Gravity wave influence on the global structure of the diurnal tide in the mesosphere and lower thermosphere. *J. Geophys. Res.* 111, A10S10. <http://dx.doi.org/10.1029/2005JA011467>.
- Palmeiro, F.M., Barriopedro, D., García-Herrera, R., Calvo, N., 2015. Comparing sudden stratospheric warming definitions in reanalysis data. *J. Clim.* 28, 6823–6840. <http://dx.doi.org/10.1175/JCLI-D-15-0004.1>.
- Pancheva, D., Mukhtarov, P., Mitchell, N.J., Merzlyakov, E., Smith, A. K., Andonov, B., Singer, W., Hocking, W., Meek, C., Manson, A., Murayama, Y., 2008. Planetary waves in coupling the stratosphere and mesosphere during the major stratospheric warming in 2003/2004. *J. Geophys. Res.* 113 (D12), D12105. <http://dx.doi.org/10.1029/2007JD009011>.
- Pancheva, D., Mukhtarov, P., Andonov, B., Mitchell, N.J., Forbes, J.M., 2009. Planetary waves observed by TIMED/SABER in coupling the stratosphere- mesosphere-lower thermosphere during the winter of 2003/2004: Part 2—Altitude and latitude planetary wave structure. *J. Atmos. Sol.-Terr. Phys.* 71 (1), 75–87. <http://dx.doi.org/10.1016/j.jastp.2008.09.027>.
- Pascoe, C.L., Gray, L.J., Crooks, S.A., Juckes, M.N., Baldwin, M.P., 2005. The quasi-biennial oscillation: analysis using ERA-40 data. *J. Geophys. Res.* 110, D08105. <http://dx.doi.org/10.1029/2004JD004941>.

- Phillips, D.S., 1984. Analytical surface pressure and drag for linear hydrostatic flow over three-dimensional elliptical mountains. *J. Atmos. Sci.* 41, 1073–1084.
- Pogoreltsev, A.I., 1999. Simulation of planetary waves and their influence on the zonally averaged circulation in the middle atmosphere. *Earth Planets Space* 51 (7/8), 773–784.
- Pogoreltsev, A.I., 2007. Generation of normal atmospheric modes by stratospheric vacillations. *Izvestia Atmos. Ocean. Phys.* 43 (4), 423–435.
- Pogoreltsev, A.I., Kanukhina, A.Yu., Suvorova, E.V., Savenkova, E.N., 2009. Variability of planetary waves as a signature of possible climatic changes. *J. Atmos. Sol.-Terr. Phys.* 71, 1529–1539. <http://dx.doi.org/10.1016/j.jastp.2009.05.011>.
- Pogoreltsev, A.I., Savenkova, E.N., Aniskina, O.G., Ermakova, T.S., Chen, W., Wei, K., 2015. Interannual and intraseasonal variability of stratospheric dynamics and stratosphere–troposphere coupling during northern winter. *J. Atmos. Sol.-Terr. Phys.* 136, 137–200.
- Pogoreltsev, A.I., Savenkova, E.N., Pertsev, N.N., 2014. Sudden stratospheric warmings: the role of normal atmospheric modes. *Geomagn. Aeron.* 54 (3), 357–372.
- Pogoreltsev, A.I., Vlasov, A.A., Froehlich, K., Jacobi, Ch., 2007. Planetary waves in coupling the lower and upper atmosphere. *J. Atmos. Sol.-Terr. Phys.* 69, 2083–2101. <http://dx.doi.org/10.1016/j.jastp.2007.05.014>.
- Ramesh, K., Sridharan, S., Raghunath, K., Rao, S.V.B., Kumar, Y.B., 2013. Planetary wave-gravity wave interactions during mesospheric inversion layer events. *J. Geophys. Res.* 118 (7), 4503–4515. <http://dx.doi.org/10.1002/jgra.50379>.
- Reisin, E.R., Scheer, J., Dyrland, M.E., Sigernes, F., Deehr, C.S., Schmidt, C., Höppner, K., Bittner, M., Ammosov, P.P., Gavrilova, G.A., et al., 2014. Traveling planetary wave activity from mesopause region airglow temperatures determined by the network for the detection of mesospheric change (NDMC). *J. Atmos. Sol.-Terr. Phys.* 119, 71–82.
- Rice, J.A., 2006. *Mathematical Statistics and Data Analysis*, third ed. Duxbury Press, Belmont, CA.
- Quiroz, R., 1975. Stratospheric evolution of sudden warmings in 1969–74 determined from measured infrared radiation fields. *J. Atmos. Sci.* 32, 211–224. [http://dx.doi.org/10.1175/1520-0469\(1975\)032<0211:TSEOSW>2.0.CO;2](http://dx.doi.org/10.1175/1520-0469(1975)032<0211:TSEOSW>2.0.CO;2).
- Robinson, W.A., 1985. A model of the wave 1 – wave 2 vacillation in the winter stratosphere. *J. Atmos. Sci.* 41 (21), 2289–2304.
- Sassi, F., Liu, H.-L., Ma, J., Garcia, R.R., 2013. The lower thermosphere during the Northern Hemisphere winter of 2009: a modeling study using high-altitude data assimilation products in WACCM-X. *J. Geophys. Res. Atmos.* 118, 8954–8968. <http://dx.doi.org/10.1002/jgrd.50632>.
- Scheer, J., Reisin, E.R., Espy, J.P., Bittner, M., Graef, H.H., Offermann, D., Ammosov, P.P., Ignatyev, V.M., 1994. Large-scale structures in hydroxyl rotational temperatures during DYANA. *J. Atmos. Terr. Phys.* 56, 1701–1715.
- Schoeberl, M., 1978. Stratospheric warmings – observations and theory. *Rev. Geophys.* 16, 521–538. <http://dx.doi.org/10.1029/RG016i004p00521>.
- Scinocca, J.F., McFarlane, N.A., 2000. The parameterization of drag induced by stratified flow over anisotropic orography. *Quart. J. Roy. Meteorol. Soc.* 126 (568), 2353–2393.
- Sigmond, M., Shepherd, T.G., 2014. Compensation between resolved wave driving and parameterized orographic gravity wave driving of the Brewer–Dobson circulation and its response to climate change. *J. Clim.* 27 (14), 5601–5610.
- Siskind, D.E., Eckermann, S.D., McCormack, J.P., Coy, L., Hoppel, K. W., Baker, N.L., 2010. Case studies of the mesospheric response to recent minor, major and extended stratospheric warmings. *J. Geophys. Res.* 115, D00N03. <http://dx.doi.org/10.1029/2010JD014114>.
- Shaw, T.A., Shepherd, T.G., 2007. Angular momentum conservation and gravity wave drag parameterization: implications for climate models. *J. Atmos. Sci.* 64, 190–203.
- Smith, A.K., 2003. The origin of stationary planetary waves in the upper mesosphere. *J. Atmos. Sci.* 60, 3033–3041. [http://dx.doi.org/10.1175/1520-0469\(2003\)060<3033:TOOSPW>2.0.CO;2](http://dx.doi.org/10.1175/1520-0469(2003)060<3033:TOOSPW>2.0.CO;2).
- Stray, N.H., Orsolini, Y.J., Espy, P.J., Limpasuvan, V., Hibbins, R.E., 2015. Observations of planetary waves in the mesosphere-lower thermosphere during stratospheric warming events. *Atmos. Chem. Phys.* 15, 4997–5005. <http://dx.doi.org/10.5194/acp-15-4997-2015>.
- Suvorova, E.V., Pogoreltsev, A.I., 2011. Modeling of nonmigrating tides in the middle atmosphere. *Geomagnetizm Aeronomy* 51 (1), 105–115.
- Swarztrauber, P.N., Kasahara, A., 1985. The vector harmonic analysis of Laplace’s tidal equations. *SIAM J. Sci. Stat. Comput.* 6, 464–491.
- Swinbank, R., O’Neill, A., 1994. Stratosphere-troposphere assimilation system. *Month. Weather Rev.* 122, 686–702.
- Takahashi, H., Wrasse, C.M., Pancheva, D., Abdu, M.A., Batista, I.S., Lima, L.M., Batista, P.P., Clemesha, B.R., Shiokawa, K., 2006. Signatures of 3–6 day planetary waves in the equatorial mesosphere and ionosphere. *Ann. Geophys.* 24, 3343–3350.
- Valdes, P.J., Hoskins, B.J., 1989. Linear stationary wave simulations of the time-mean climatological flow. *J. Atmos. Sci.* 46, 2509–2527. [http://dx.doi.org/10.1175/1520-0469\(1989\)046<2509:LSWSOT>2.0.CO;2](http://dx.doi.org/10.1175/1520-0469(1989)046<2509:LSWSOT>2.0.CO;2).
- Vincent, R.A., 2015. The dynamics of the mesosphere and lower thermosphere: a brief review. *Prog. Earth Planet. Sci.* 2, 4. <http://dx.doi.org/10.1186/s40645-015-0035-8>.
- Vosper, S.B., Brown, A.R., 2007. The effect of small-scale hills on orographic drag. *Quart. J. Roy. Meteorol. Soc.* 133, 1345–1352.
- Watanabe, S., Miyahara, S., 2009. Quantification of the gravity wave forcing of the migrating diurnal tide in a gravity wave-resolving general circulation model. *J. Geophys. Res.* 114, D07110. <http://dx.doi.org/10.1029/2008JD011218>.
- Watson, P.A.G., Gray, L.J., 2014. How does the quasi-biennial oscillation affect the stratospheric polar vortex? *J. Atmos. Sci.* 71 (1), 391–409.
- Yamashita, Y., Akiyoshi, H., Takahashi, M., 2011. Dynamical response in the Northern Hemisphere midlatitude and high-latitude winter to the QBO simulated by CCSR/NIES CCM. *J. Geophys. Res.* 116, D06118. <http://dx.doi.org/10.1029/2010JD015016>.
- Yiğit, E., Medvedev, A.S., 2015. Internal wave coupling processes in Earth’s atmosphere 55(4), 983–1003. <http://dx.doi.org/10.1016/j.asr.2014.11.020>.
- Yuan, T., Thurairajah, B., She, C.-Y., Chandran, A., Collins, R.L., Krueger, D.A., 2012. Wind and temperature response of midlatitude mesopause region to the 2009 sudden stratospheric warming. *J. Geophys. Res.* 117, D09114. <http://dx.doi.org/10.1029/2011JD017142>.